



Total Control

Upgrade of the Dynamic Wake Meandering model

Title (of deliverable): Upgrade of DWM
Deliverable no.: D1.6

Delivery date: 15.01.2019
Lead beneficiary: Gunner Chr. Larsen
Dissemination level: PU



This project has received funding from the European Union's Horizon 2020 Research and Innovation Programme under grant agreement No. 727680

Author(s) information (alphabetical):

Name	Organisation	Email
Gunner Chr. Larsen	DTU	gula@dtu.dk
Paul van der Laan	DTU	
Søren Juhl Andersen	DTU	

Acknowledgements/Contributions:

Name	Name	Name

Document information

Version	Date	Description			
			Prepared by	Reviewed by	Approved by
1	15.01.2019	Name	G.C. Larsen		J. Meyers

Definitions

DWM	Dynamic Wake Meandering
WT	Wind turbine
WF	Wind farm
ABL	Atmospheric boundary layer
CFD	Computational fluid mechanics
RANS	Reynolds averaged Navier Stokes
LES	Large eddy simulation

TABLE OF CONTENTS

Executive summary	4
Introduction	4
DWM Classic.....	5
DWM with buoyancy effects included.....	7
3.1 Basic conjecture	7
3.2 Synthetic ABL turbulence modeling accounting for buoyancy effects.....	9
3.3 ABL shear under non-neutral conditions	10
3.4 ‘Validation’	13
3.4.1 The Lillgrund case	13
3.4.2 The measurements	13
3.4.2 The simulations	14
3.4.3 The results	16
3.4.4 The conclusion	19
DWM in flow fields influenced by WT yawing	19
4.1 Wake advection path and wake deficit.....	19
4.1.1 RANS based investigations	20
4.1.2 LES based investigations.....	23
4.2 Full-scale observations of flow fields behind a yawed WT.....	25
4.3 DWM for yawed operation of WT’s	26
Conclusions	28
References	28

EXECUTIVE SUMMARY

The Dynamic Wake Meandering (DWM) model is a cost efficient way to model non-stationary wind farm (WF) flow fields. Non-stationary WF flow fields are needed for prediction of loads of wind turbines (WT's). The DWM model is a medium-fidelity model. Medium-fidelity modelling offers an attractive alternative to high-fidelity modelling, when a large number of flow cases is to be simulated as e.g. in the context of optimization.

In TotalControl we aim at including WT loading in designing optimal WF control schemes. The first version of the DWM model was limited to neutral atmospheric conditions and zero yaw error of the WF WT's. The present report describes two important extensions of the original DWM model - 1) extension to non-neutral atmospheric stability; and 2) inclusion of possible WT yaw errors. Extension 1) is important because WT loading known to depend on atmospheric stability. Extension 2) is important because individual WT wake-steering (i.e. WT yaw control), besides WT de-rating, is a traditional approach used for optimal WF control.

First the basic elements of the 'classic' DWM model is outlined. Then the generalization of neutral to non-neutral atmospheric conditions are described. This involves both a modification of the relevant turbulence fields and the vertical mean wind shear, since now both surface friction and buoyancy contributes to turbulence generation. The capability of the resulting model is validated against an extensive set of full-scale load data from the Lillgrund WF.

The generalization of the DWM model to cope with yawed WT's involve re-definition of wake downstream advection paths. Such paths are obtained based on CDF simulations, and a 'indicative' validation of these are performed using a single full-scale event resolved using an advanced LiDAR based technology. In addition to the downstream advection path, the wake deficit modelling as well as the modelling of the self-generated small-scale wake turbulence needs modification.

INTRODUCTION

The DWM model [1] was introduced in 2008 as a *medium-fidelity* model that was able to respond on the need for a 'consistent' model which, in combination with an aeroelastic model, could facilitate prediction of power production as well as non-stationary loading of WT's located in WF's. Since then validation has been ongoing using 'metrics' based on flow characteristics [2 - 4] as well derived quantities such as WT production [5] and WT fatigue loading [5 - 6]. The DWM model is now well established and is recently included in the new edition of the IEC standard [7] as a recommended practice for load prediction of WT's subjected to wake affected flows.

In the DWM model, the flow field is based on Reynolds decomposition, where a mean flow field is superimposed by a flow field fluctuating in time and space. In case the flow field in question is the atmospheric boundary layer (ABL), the fluctuating part is traditional turbulence. However, in the case WF flow fields the fluctuating part has pronounced intermittent characteristics caused by interacting WT wakes superimposed linearly on conventional ABL turbulence. Such WT wake consists, in the context of the DWM model, of a velocity deficit superimposed by a wake self-generated turbulence field, and both the wake deficit and the self-generated turbulence field are described in a stochastically moving 'meandering frame of reference'.

The 'classic' DWM model assumes *neutral* atmospheric stratification. Therefore, the mean flow field are conveniently described by a logarithmic shear profile [8]. However, neutral stratification only prevails a fraction of the lifetime of WT's, and it is therefore important to be able to simulation flow conditions associated to stable- and unstable stratification of the ABL. This is especially important for prediction of WT loading.

The loading of an operating WT depends on both mean wind field characteristic and characteristics of the fluctuating part of the flow imposed on a WT, which in turns mean that the dependence of both the mean and the fluctuating flow field with atmospheric stability must be considered. This is the topic for the first part of the report, in which the 'classic' DWM model is briefly described in Chapter 2 in order to provide a basis for the generalization of the model to non-neutral ABL stratification outlined in Chapter 3.

Another type of generalization is in focus in Chapter 4 of this report. This relates directly to the overall theme of the control project - WF control. Basically, two approaches can be taken in this regard: 1) WT de-rating, where (some) individual WT's sacrifice performance (e.g. power production) to the benefit of the performance of the entire WF; 2) Active yaw control, where the philosophy is to re-direct upstream emitted wakes by yawing the associated upstream WT's. The 'classic' DWM model does not consider (significant) yaw of upstream WT's. This is why a generalization of the DWM model is needed to include aspects related to the latter approach.

DWM CLASSIC

The fundamental conjecture behind the DWM model [1] is that wakes can be considered as *passive tracers* consecutively released from upstream WT's and subsequently Taylor advected downstream under the influence of large scale turbulence structures in the lateral and vertical directions. Model vice, this is achieved by a convenient *split in scales*, where 'big' turbulence scales are responsible for wake dynamics, whereas 'small' turbulence scales dictates wake diffusion (i.e. wake expansion and wake attenuation) with downstream distance.

Although not formally correct, the DWM model is sometimes denoted as 'the poor man's LES'. The analogy to CFD LES is the following: The 'big' turbulence scales dictating the wake kinematics in the lateral- and vertical directions is, in the DTU implementation, based on the Mann spectral tensor [9], which is consistent with a linearization of the Navier-Stokes (N-S) equations, whereas the advected wake deficits (i.e. the small scales in the DWM context) is simulated as based on an eddy viscosity closure.

The DWM model considers wakes as *linear perturbations* on the ambient non-uniform mean wind field, although the modelling of the individual quasi-steady wake flow structures includes non-linear terms. The model is composed of three parts: 1) A model of the *wake deficit* formulated in the meandering frame of reference; 2) A stochastic model of the downstream wake *meandering process*; and 3) A model of the self-induced *wake turbulence* described in the meandering frame of reference. These three basic elements of the model are illustrated in Figure 1 below.

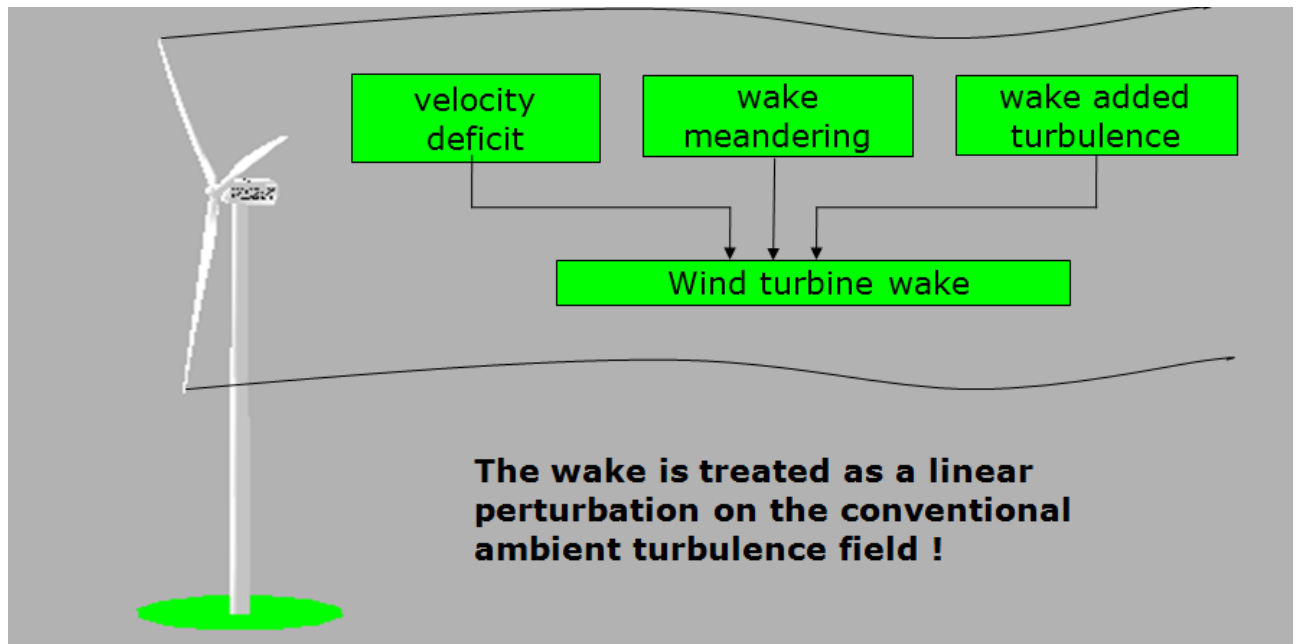


Figure 1: - The three fundamental parts of the DWM model.

The *mean wake deficit* is an organized flow structure, which expands and attenuates with the downstream distance from the wake generating rotor. The modeling of the *wake deficit* is, in the DTU implementation, based on a solution of the thin shear layer approximation to the N-S equations adopting an eddy viscosity approximation for the Reynolds stresses. The eddy viscosity formulation contains contributions from both ABL turbulence and the wake self-generated turbulence [10]. The wake flow field structure are assumed *rotationally symmetric*, and the rotor inflow field is consistently assumed uniform - in practice equal to the rotor-averaged inflow. This approach is not mandatory, but could also be modeled in more detail for example using a CFD actuator disc model and a sheared inflow field.

The *wake meandering* part is based on the fundamental presumption that the transport of wakes in the atmospheric boundary layer can be realistically approximated by considering the wakes to act as *passive tracers* (despite the fact that their content of momentum deviates from the momentum of the ambient flow) driven by the *large-scale* turbulence structures. Modeling of the meandering process consequently includes considerations of a suitable description of the stochastic 'transport media' (i.e. the large scale turbulence field) as well as of a suitable definition of the cut-off frequency defining large-scale turbulence structures in this context. The stochastic modeling of wake meandering is established by considering a *cascade* of wake deficit releases 'emitted' at consecutive time instants in agreement with the passive tracer analogy. The propagation of each 'emitted' wake deficit is subsequently modeled, and the collective description of these constitutes the wake meandering model in space and time.

Wake induced turbulence includes contributions from conventional mechanically generated turbulence, caused by the wake shear, as well as from the blade shed and trailed vortices mainly in terms of tip and root vortices gradually breaking down downstream of the wake generating rotor. With a length scale comparable with the characteristic size of the wake deficit [11], the basic DWM split in scales implies that the wake induced turbulence meanders together with the wake deficit. The induced small-scale turbulence is consequently - like the wake deficit - formulated in the meandering frame of reference. Although violating the second order statistics

(i.e. the cross correlation properties), the *in-homogeneity* of the induced turbulence is approximated by *simple scaling* of a homogeneous and isotropic turbulence field with a length scale equal to one rotor diameter. *Rotational symmetry* of the self-generated wake turbulence *intensity* is assumed, which is consistent with the assumed rotational symmetry of the wake deficit.

The proposed medium-fidelity formulation of WF flow fields accounts for changes in the mean flow field over the wind farm as well as for changes in the turbulence *intensity* and turbulence *structure* compared to ambient conditions.

DWM WITH BUOYANCY EFFECTS INCLUDED

To generalize the DWM model to deal with stable- and unstable stratification of the ABL, we note that both *mean wind shear* and turbulence *intensity* and turbulence *structure* changes compared to neutral ABL conditions. The turbulence generation, and thereby the turbulence characteristics, is changed because buoyancy forces now add to friction forces, with the former mainly affecting the large-scale turbulence structures [8]. As a consequence the the mean shear is modified - larger mixing under unstable ABL stratification leads to less mean wind shear, and less mixing for stable ABL stratification leads to more pronounced mean wind shear. The mean wind shear is strictly speaking not a part of the DWM model, but should be considered as an element of the ambient flow. The reason it is included here, is that vertical mean wind shear plays an important role for the dynamic loading of rotating WT components, and further that the classic Monin-Obukhov shear corrections formulas turn out to insufficient outside the surface layer, where most modern WT's are operating.

3.1 BASIC CONJECTURE

As ABL stability mainly affects the large scale turbulence structures, the effect of buoyancy on wake meandering can obviously not be neglected. In addition, the significance of buoyancy effects on small turbulence structures relevant for wake deficit expansion and attenuation in the meandering frame of reference must be clarified. The crucial question in this respect is whether the effect of buoyancy can be 'decomposed' in analogy with the DWM split-in-scale description of wake dynamics for a neutral ABL.

Investigations based on full-scale LiDAR recordings [12] lead to the following the following fundamental conjecture: *In a wake context, ABL stability affects primary wake meandering - driven by large (lateral and vertical) turbulent scales - whereas the effect on wake expansion and attenuation, in the meandering frame of reference, is only of second order importance.*

Justification of the above-mentioned conjecture is illustrated in Figures 2 and 3 below.

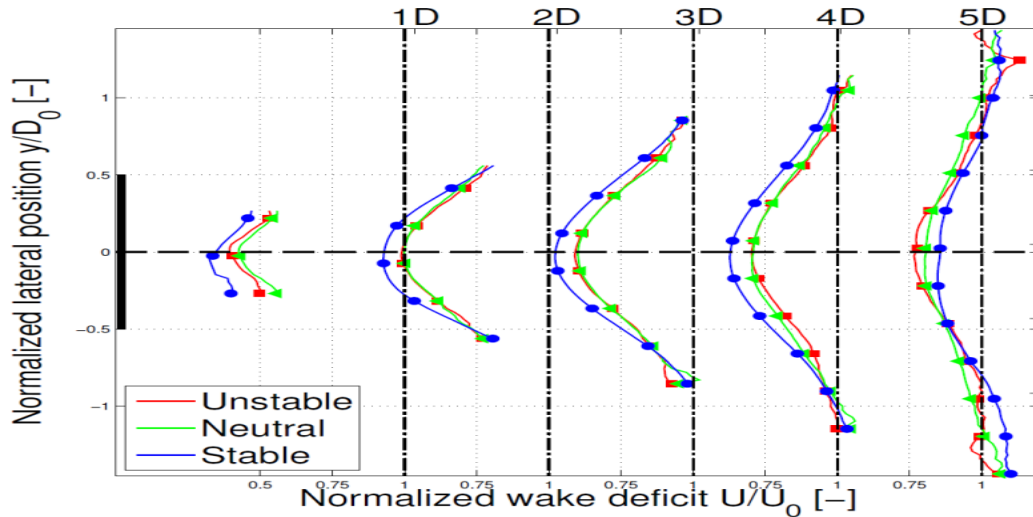


Figure 2: Normalized wake deficits in the meandering frame of reference shown for three different ABL stability conditions.

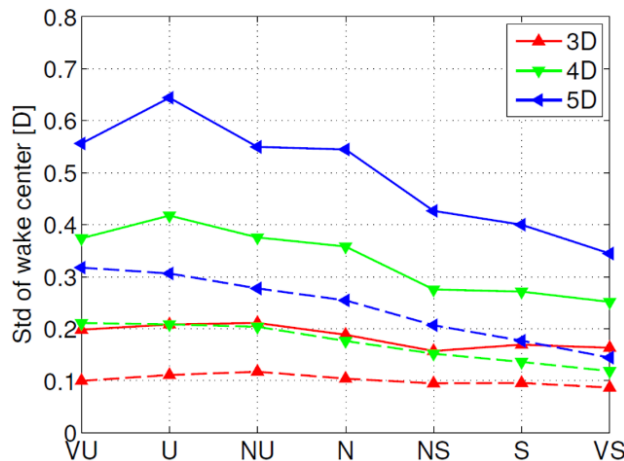


Figure 3: Intensity of lateral- and vertical wake meandering for three different ABL stability conditions.

The flow field behind a 500kW Nordtank WT was resolved using a pulsed LiDAR mounted on the WT nacelle and scanning downstream, thus simultaneously resolving 5 cross sections at downstream distances ranging from 1 rotor diameter (D) to 5D. Various ABL stability conditions was investigated for approximately identical ambient wind speed conditions ranging from 6.8m/s to 7m/s.

Figure 2 shows the wake deficits normalized with the ambient mean wind speed at hub height resolved in the meandering frame of reference (MFoR) for three different ABL stability conditions - stable, neutral and unstable. The wakes 1D and 2D downstream are only partly resolved because of limited opening angle of the LiDAR equipment. Figure 3 shows the standard deviation of the wake center displacement given in D as function of the ABL stability characteristics (VU: very unstable; U: unstable; NU: near neutral unstable; N: neutral; NS: near neutral stable; S: stable; VS: very stable). The dotted lines refer to vertical wake displacement, whereas the full lines symbolize lateral wake displacement. As seen, there is a strong dependence between ABL stability conditions and (especially lateral) wake meandering. As for the wake deficits resolved

in the MFOR, the wake deficits associated with neutral- and unstable ABL conditions are almost identical, whereas minor deviations are observed for stable ABL conditions.

Based on the introduced conjecture a direct link from ABL stability to the original DWM split-in-scale approach is established. The strategy is thus to replace the Mann spectral tensor modeling of the turbulence scales responsible for the wake meandering with a turbulence modeling accounting for buoyancy. This is described in the following section.

3.2 SYNTHETIC ABL TURBULENCE MODELING ACCOUNTING FOR BUOYANCY EFFECTS

In this section a generalization of the Mann spectral tensor to a spectral tensor, which consistently include buoyancy effects is briefly outlined [13 - 15].

The generalized spectral tensor, $\Phi_{ij}(\mathbf{k})$, resulting from the governing Rapid Distortion Theory (RDT) equations including the buoyancy effects contains two extra parameters, in addition to those of the “classic” Mann spectral tensor model, where $\mathbf{k}(t) = (k_1, k_2, k_{30}-k_1(dU/dz)t)$ is a three dimensional wave vector, and t is time. These parameters are: 1) a stability parameter (the Richardson number) and 2) the rate of destruction of temperature variance.

The RDT equations, which include the linearized momentum and the temperature equation in Fourier space, evaluates in time under the influence of a *constant wind shear* (dU/dz) and a *constant gradient* of potential temperature ($d\theta/dz$) from an initial isotropic state of turbulence. In isotropic turbulence, the velocity-spectrum tensor is

$$\Phi_{ij}(\mathbf{k}_0) = \frac{E(k)}{4\pi k^2} \left(\delta_{ij} - \frac{k_i k_j}{k^2} \right), \quad (1)$$

where $\mathbf{k}_0 = \mathbf{k}(0)$ and k is the magnitude of the vector \mathbf{k} . The energy spectrum, $E(k)$, is given by [16] as

$$E(k) = \alpha \varepsilon^{2/3} L^{5/3} \frac{(kL)^4}{(1 + (kL)^2)^{17/6}}, \quad (2)$$

where $\alpha \approx 1.7$ is the Kolmogorov constant, ε is the rate of viscous dissipation of specific turbulent kinetic energy (TKE), and L is a turbulence length scale.

In order to make the model stationary, the time dependency in the model is removed by incorporating the general concept of an eddy life time, $\tau(k)$. The parameterization of $\tau(k)$ is adapted from the “classic” Mann spectral tensor model [9]. In the inertial sub-range, the life time of eddies are proportional to $k^{-2/3}$, and the assumption in the Mann model, for scales larger than the inertial sub-range, is that the eddy life time is proportional to k^{-1} divided by their characteristic velocity given by

$$\left(\int_k^\infty E(p) dp \right)^{1/2}, \quad (3)$$

thus resulting in eddy life times proportional to $k^{-2/3}$ for $k \rightarrow \infty$ and to k^{-1} for $k \rightarrow 0$.

For the temperature variable, the isotropic three-dimensional spectrum is given as

$$\Phi_{\theta\theta}(\mathbf{k}_0) = \frac{S(k)}{4\pi k^2}, \quad (4)$$

where $S(k)$ is the potential temperature energy spectrum containing the form of the inertial sub-range [13] as

$$S(k) = \beta \varepsilon^{-1/3} \varepsilon_\theta L^{5/3} \frac{(kL)^2}{(1 + (kL)^2)^{11/6}}, \quad (5)$$

Here ε_θ is the dissipation rate for half the temperature variance, and $\beta = 0.8$ is a universal constant [13]. Based on the above formulations of isotropic velocity and temperature spectra combined with the Mann eddy life time formulation, RTD results in an anisotropic spectral tensor including buoyancy of the form $\Phi_{ij}(\mathbf{k}) = \Phi_{ij}(\mathbf{k}; \alpha \varepsilon^{2/3}, L, \Gamma, Ri, \eta_\theta)$, where Ri denotes the Richardson number [8] resulting from the temperature equation, and

$$\eta_\theta \equiv \frac{\varepsilon_\theta}{\varepsilon} \left[\frac{g}{\theta} \left(\frac{dU}{dz} \right)^{-1} \right]^2, \quad (6)$$

where the potential temperature, θ , as well as dU/dz and $d\theta/dz$ are representative of the height of interest. To summarize, the five adjustable model parameters, which are attainable from *single-point measurements* are: 1) $\varepsilon^{2/3}$; 2) L , which represents a representative size of the energy containing eddies; 3) Γ , which is a measure of the degree of turbulence isotropy; the Richardson number Ri ; and 5) η_θ as defined above. Note, that for $Ri = 0$ and $\eta_\theta = 0$, the generalized spectral tensor degenerates to the ‘classic’ Mann spectral tensor.

Simulation of consistent 3D synthetic turbulence fields requires knowledge of cross-spectra between turbulence components. The spectral tensor model provides the cross-spectrum, χ_{ij} , between any two velocity components, or between any velocity component and temperature, as

$$\begin{aligned} \chi_{ij}(k_1, \Delta y, \Delta z; \alpha \varepsilon^{2/3}, L, \Gamma, Ri, \eta_\theta) \\ \equiv \alpha \varepsilon^{2/3} L^{5/3} \int \Phi_{ij}(\mathbf{k}; \alpha \varepsilon^{2/3}, L, \Gamma, Ri, \eta_\theta) e^{i(k_2 \Delta y + k_3 \Delta z)} dk_2 dk_3, \end{aligned} \quad (7)$$

where Δy and Δz are transverse and vertical separations, respectively. Thus, based on such cross-spectra, the requested turbulence field is simulated using an approach similar to the approach described in [17].

For given site conditions, the 5 model parameters may be fitted from single-point measurements using an automated fit procedure as based on a chi-squared (χ^2) fitting technique similar to the one applied for the classic Mann spectral tensor [9]. The basic idea of the χ^2 fit is to minimize the sum of the squared differences between the theoretical and the estimated spectra and co-spectra. Compared to fitting of model parameters of the classic spectral tensor the χ^2 function, corresponding to the generalized spectral tensor, is expanded by including the θ auto-spectrum as well as the $u\theta$ and $w\theta$ co-spectra.

3.3 ABL SHEAR UNDER NON-NEUTRAL CONDITIONS

Having the turbulence simulation in place, we now turn to (vertical) shear for non-neutral ABL conditions [21, 22]. Initially, we confine our efforts to flows over *flat* and *homogeneous terrain*. To be more precise, we are talking about a rough surface with evenly distributed roughness elements (vegetation, buildings, waves etc.) that make the terrain homogeneous in a statistical sense. In the vicinity of the roughness elements, sometimes referred to as the buffer layer, the flow depends on the detailed shape of the surface and therefore does not have a universal character. However, just above the buffer layer a logarithmic layer is always found. In neutral conditions the logarithmic layer extends through the whole surface layer, while the logarithmic wind profile is modified in the upper part of the surface layer in both stable and unstable conditions.

The vertical mean wind speed profile is stability dependent through the impact of buoyancy on mixing in the ABL layer – in stable conditions with little/suppressed mixing the gradient of vertical mean wind speed profile tend to increase, whereas in unstable conditions, with increased mixing, the vertical mean wind speed profile tend to become more uniform.

Within the surface layer the *Monin-Obukhov (M-O) scaling theory* has proven very successful and is widely used. Adopting the physically consistent logarithmic profile for the neutral case and neglecting the influence of boundary layer height, the M-O formulation of the *non-neutral* vertical mean wind speed profile, U , may be expressed as [8].

$$U_{MO}(z, z_0, L_M) = \frac{u_*}{\kappa} \left[\text{Ln} \left(\frac{z}{z_0} \right) - \psi_m \left(\frac{z}{L_M} \right) \right], \quad (8)$$

where u_* is the friction velocity, z_0 is the roughness length, L_M is the M-O scaling length, and $\kappa = 0.41$ is the von Karman constant. The celebrated stability function, ψ_m , has unstable- and stable branches, respectively.

The vertical mean wind speed profile may, under *unstable conditions*, be formulated as [8, 35]

$$U_{MO}(z, z_0, L_M) = \frac{u_*}{\kappa} \left[\text{Ln} \left(\frac{z}{z_0} \right) - \text{Ln} \left[\frac{1+x^2}{2} \left(\frac{1+x}{2} \right)^2 \right] + 2A \tan(x) - \frac{\pi}{2} \right]; \quad (9)$$

$$-2 \leq z/L_M < 0;$$

$$x = \left(1 - 16 \frac{z}{L_M} \right)^{1/4}$$

The analog expression for the vertical mean wind speed profile under *stable conditions* is given by [8]

$$U_{MO}(z, z_0, L_M) = \frac{u_*}{\kappa} \left[\text{Ln} \left(\frac{z}{z_0} \right) + 5 \frac{z}{L_M} \right]; 0 < z/L_M \leq 1 \quad (10)$$

Classic M-O scaling is in principle limited to the surface layer. This has been challenged in a recent study [22], where a thorough investigation of 3 Danish offshore sites (Horns Reef; Nysted; and Læsø) *outside* the surface layer has been conducted. The investigation demonstrates that mean wind speeds in *unstable* cases are remarkably well predicted by the classic surface layer M-O similarity theory even outside the surface layer. In *stable* cases, however, some *large over-predictions* were observed, especially for low mean wind speeds under strongly stable conditions (cf. Figure 4a).

The failure of conventional M-O theory in (some) stable cases has led to the development of an extended version of the M-O theory, in which a correction to the classic M-O theory for *stable* conditions is re-formulated. For derivation of the extended M-O theory we refer to The developed extended M-O theory has been validated against full-scale meteorological observations. Convincing agreement between model predictions and full-scale data has been demonstrated in altitude the regime ranging from 62m and up to 900m using data from 3 Danish offshore sites as well as from the German Fino platform, and it is concluded that the model is behaving surprisingly well even for heights elevated high above the surface layer (cf. Figure 4b).

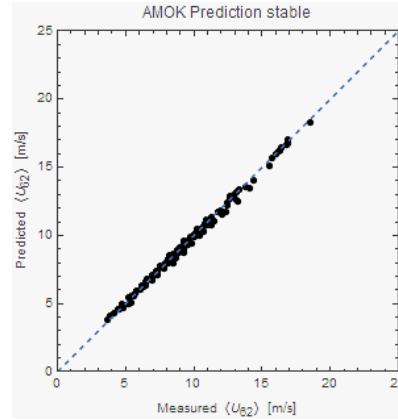
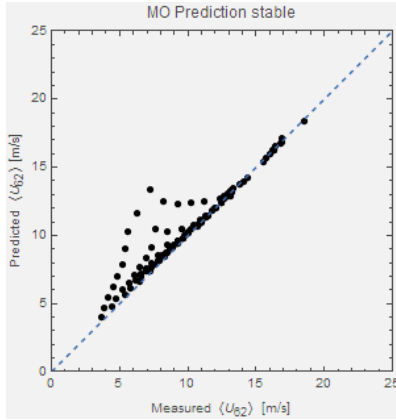


Figure 4a: Predicted *classic* M-O vs. measured values of bin averaged U_{62} . Horns Reef at 62m altitude.

Figure 4b: Predicted *extended* M-O vs. measured values of bin averaged U_{62} . Horns Reef at 62m altitude.

To describe the extended M-O theory we re-write eq. (10) as

$$\begin{aligned} U_{MO}(z, z_0, L_M) &= \frac{u_*}{\kappa} \left[\text{Ln} \left(\frac{z}{z_0} \right) - \psi_m^{(s)} \left(\frac{z}{L_M} \right) \right] \\ &= \frac{u_*}{\kappa} \left[\text{Ln} \left(\frac{z}{L_M} \right) - \text{Ln} \left(\frac{z_0}{L_M} \right) - \psi_m^{(s)} \left(\frac{z}{L_M} \right) \right] \end{aligned} \quad (11)$$

where upper index '(s)' indicates the stable branch of the on the stability correction function. Introducing non-dimensional variables

$$\tilde{z} = \frac{z}{L_M}; \quad \tilde{z}_0 = \frac{z_0}{L_M} \quad (12)$$

eq. (11) may be reformulated as

$$U_{MO}(\tilde{z}, \tilde{z}_0) = \frac{u_*}{\kappa} \left[\text{Ln}(\tilde{z}) - \text{Ln}(\tilde{z}_0) - \psi_m^{(us)}(\tilde{z}) \right] \quad (13)$$

The extended M-O theory, developed in [22], expresses the vertical mean wind speed profile under *stable conditions* as

$$U_{EMO}(\tilde{z}, \tilde{z}_0, \mu) = \frac{U_{MO}(\tilde{z}, \tilde{z}_0)}{\sqrt{1 + b\tilde{z}^2/\mu}} \quad (14)$$

with μ being the Monin-Kazanski parameter (the non-dimensional Coriolis parameter) defined by

$$\mu = \frac{u_*}{fL_M} \quad (15)$$

where f is the Coriolis parameter defined by

$$f = 2\Omega \text{Sin}(\varphi) \quad (16)$$

Ω is the rotation rate of the Earth, and φ is the latitude. At Lillgrund location $f = 1.914 \times 10^{-5}$ Hz.

3.4 'VALIDATION'

Siemens has made available recorded WT load data for a period of almost 5 years; i.e. a measurement period extends from 2008-06-03 to 2013-03-19. – i.e. over a period of almost 5 years. The measurements are from the Lillgrund WF with a layout characterized by very small WT inter spacing's – i.e. down to 3.3 D. This makes the Lillgrund WF especially interesting and challenging as a wake-load validation case, because the close spacing magnifies wake generated load effects compared to more traditional spaced WF's. A huge scatter in the measured load data was observed, and to investigate whether at least part of this scatter can be attributed to ABL stability effects, the DWM model, generalized to non-neutral ABL conditions, was used together with the state-of-the-art multi-body aeroelastic code HAWC2 to simulate the measured loads for various ambient wind speeds and inflow directions [21].

3.4.1 THE LILLGRUND CASE

The Lillgrund WF consists of 48 Siemens SWT-2.3-93 WT's. The layout of the WF is shown in Figure 5 along with the location of the Drogden light tower.

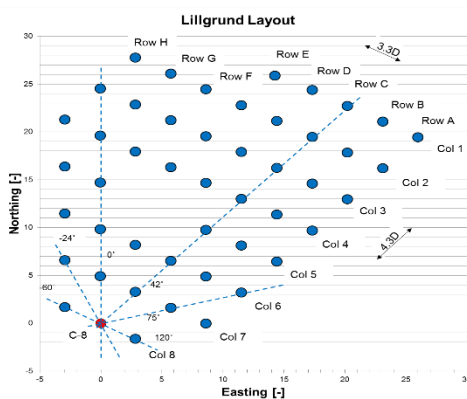


Figure 5: Layout of the Lillgrund WF with the instrumented WT C-8 marked. Distances are non-dimensional with the rotor diameter. Also shown is Drogden light tower located WNW of the WF. The distance between WF and the light tower roughly corresponds to a characteristic scale of the WF.

3.4.2 THE MEASUREMENTS

One of the Lillgrund WT's (C-8) is instrumented with strain gauges resolving respectively the blade root flap bending moment, two main shaft bending moments and the tower base fore-aft bending moment. These measurements constitute probably one of the most comprehensive sets of wake affected wind turbine load measurements ever recorded.

In addition to these high-frequency data, WT SCADA data (pitch setting, rotational speed and electrical power) were available for the WF WT's during the measuring period. Unfortunately no meteorological mast data was available within the recording period, but as the WT power and pitch angle are directly correlated with the inflow wind speed, the ambient undisturbed wind speed has been estimated as based on power and pitch angle recordings for corner placed WT's located in free inflow conditions. A similar philosophy was used for estimating the ambient undisturbed wind direction, which was determined from nacelle orientations of corner placed WT's. These nacelle orientations were initially calibrated against power deficit polar's constrained to directions where wake losses were dominated by the closest neighboring WT's. To facilitate stability classification, meteorological data from the nearby Drogden light tower was offered for the investigation. This light tower is located a few kilometers WNW of the WF, and

with the distance being of the same order of magnitude as the extension of the WF, the light tower meteorological data are deemed applicable for stability classification of the WF structural data. The data set holds approximately 15.600 hours of measurements covering the period 2008–2013. Like the structural data, the light tower data are organized as 10-minute recordings, and 10-minute mean values of wind speed and temperature at 22m altitude as well as water temperature 1m below mean sea level (MSL) was available.

As for the structural data, full polar load cases, associated with normal WT operation, are available for mean wind speeds ranging from 6m/s to 16m/s. Data binning in 3 dimensions – mean wind speed; mean wind direction; and ABL stability class – is quite demanding and requires a huge set of data. The desire of smallest possible bins has to be balanced against sufficient ‘data population’ of each individual bin, and in the end it was decided to use 2m/s bins for the mean wind speed and 4 degree bins for the wind direction. The ABL stability was classified according to Table 1, which is obtained from the suggested stability classification in [18] by collapsing these stability classes into only 3 classes.

Table 1: ABL stability classification in terms of Monin-Obukhov length L_M .

Description	Stability identifier	Condition
Unstable	-2	$-200\text{m} < L_M < -50\text{m}$
Neutral	0	$200\text{m} < L_M $
Stable	2	$10\text{m} < L_M < 200\text{m}$

The blade root flap moments and the tower bottom for-aft moments have been post processed to fatigue equivalent moments using the Palmgren-Miner [19] approach and subsequently normalized with the respective fatigue equivalent moments associated with an inflow wind speed of 9m/s – i.e. here represented by mean equivalent moments associated with the velocity bin [8;10]m/s. Wöhler exponents of 4 and 10 were assumed for the tower and blade composite structures, respectively.

3.4.2 THE SIMULATIONS

For the DWM/HAWC2 validation study the load response of WT C-8 is simulated for mean wind speeds reflecting the median of the velocity bins defined for the measurements. Measured wind speed dependent turbulence intensities (TI's) are used, reflecting the offshore wind speed dependent ‘surface’ roughness. However, no attempt is done to resolve TI as function of upstream fetch (i.e. direction). Thus, for the mean wind speed 6m/s a TI of 5.8% is used – gradually increasing to 6.2% at 16m/s.

Mean wind shear

Because site meteorology measurements, facilitating derivation of the site mean wind speed vertical profile, doesn't exist, it was decided to use the IEC offshore wind shear profile as a surrogate for the *neutral* profile in the analysis. The IEC offshore profile is specified in terms of a power exponent α equal to 0.14 [23]. To recast this profile into the more physically sound log-formulation described in Section 3, we approximated a log-profile to the IEC power law profile. Specifically, the best possible agreement of respectively the power law profile and log profile over the vertical extent of the rotor was requested, and this ‘best’ fit was defined in terms of minimum least square metric Π . Thus

$$\Pi(z_0) = U_{hub}^2 \int_{z_{hub}-R}^{z_{hub}+R} \left[\frac{\ln(z/z_0)}{\ln(z_{hub}/z_0)} - \left(\frac{z}{z_{hub}} \right)^\alpha \right]^2 dz \quad (17)$$

where the requested roughness, z_0 , are defined the particular value that minimizes Π ; viz.

$$\hat{z}_0 = \left\{ \hat{z}_0 \mid \Pi(\hat{z}_0) = \min_{z_0} \{ \Pi(z_0) \} \right\} \quad (18)$$

Adopting the roughness defined in eq. (18), the vertical mean wind speed profile for the non-neutral ABL stability conditions was evaluated using eqs. (9) and (14) for the unstable- and the stable ABL regime, respectively.

Turbulence

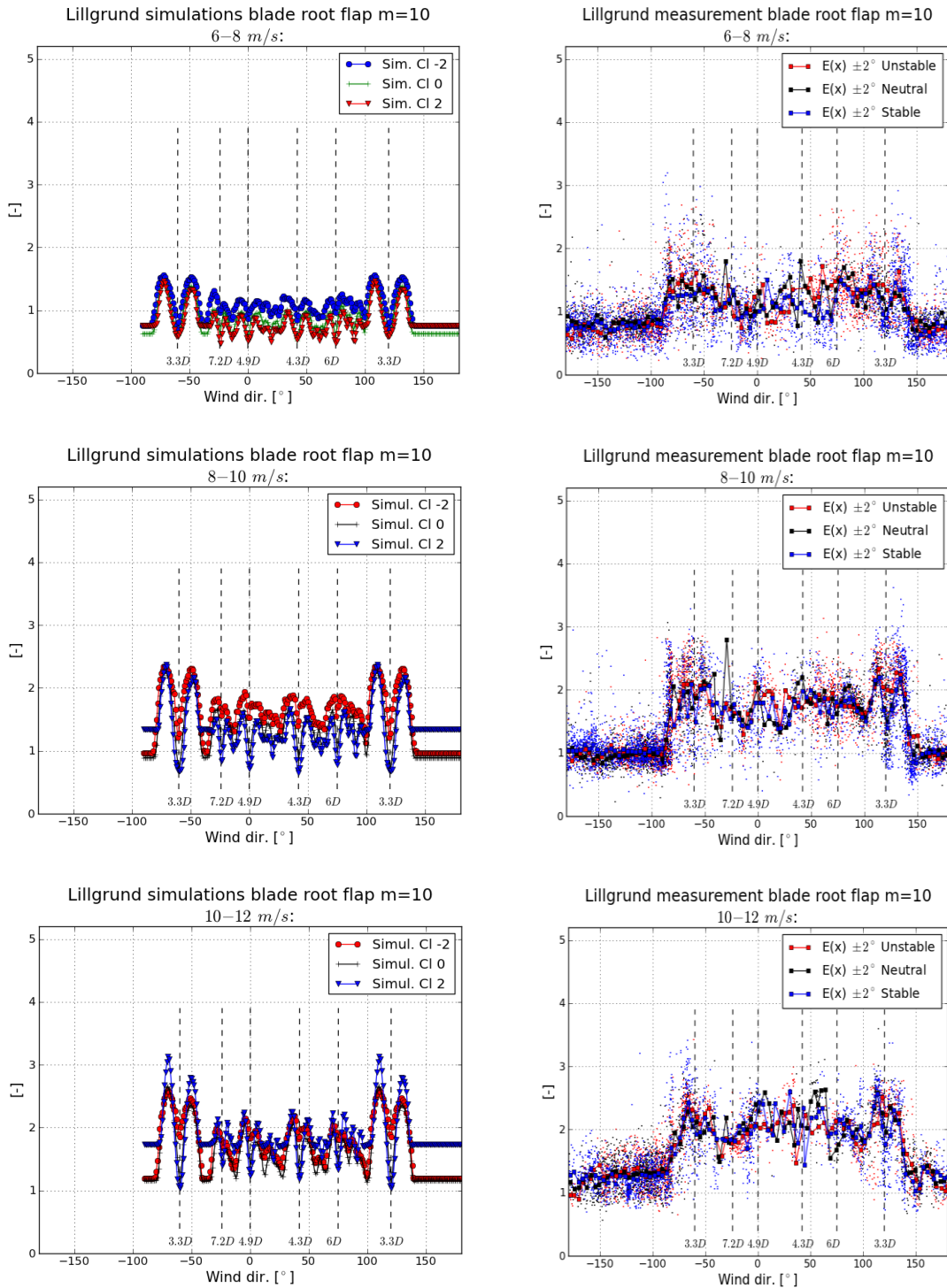
The coupled DWM-HAWC2 platform [10] requires simulation of three different turbulence fields – a large scale turbulence field dictating the wake meandering, a traditional turbulence field accounting for conventional ABL WT turbulence loading, and an *isotropic* and *inhomogeneous* small scale turbulence field accounting for WT loading caused by wake self-generated turbulence. The wake self-generated turbulence field is *assumed* to be invariant with respect to the ABL stability condition, and it is simulated using the classic Mann turbulence simulator [17]. The two remaining turbulence fields, which are highly dependent on ABL stability conditions, are generated based on the generalized buoyancy dependent spectral tensor. In all cases the turbulence fields are simulated as three dimensional fields resolved in suitable Cartesian grid configurations.

The parameters of the buoyancy dependent spectral tensor are, for each stability class, obtained from fitting model auto- and cross spectra to respective spectra obtained from full-scale sonic measurements from the Høvsøre site in Denmark. Data associated with the [8;9]m/s mean wind speed bin were used for the parameter fitting due to the good data coverage. Of the available sonic measurements, it was decided to base the fitting on data from a sonic located at 40m altitude, because this sonic is more likely to be within the surface layer, where L_M is defined, than the sonic's located at higher alternative altitudes (especially for stable stratification). Moreover, the model fitting to data at this altitude seems to slightly to outperform the fits to alternative sonic data.

Except for the turbulence intensity (described by the $\alpha \varepsilon^{2/3}$ parameter of the spectral tensor *when* the remaining parameters have been fixed), it was further decided to adopt the (neutral) turbulence input specifications from the IEC code [7] to mimic the turbulence conditions at the Lillgrund site, where no high-frequency meteorological measurements, as mentioned, are available. The IEC spectral tensor input parameters were originally obtained by fitting the spectral tensor spectra to a target Kaimal spectra. Since we have decided to base the neutral turbulence generation partly on IEC specifications of turbulence tensor input (i.e. turbulence length scale L and eddy life time parameter Γ), the spectral tensor input parameters for neutral conditions do not match the fitted parameter values from the Høvsøre full-scale data. As a consequence, it was decided to scale (L , Γ) for the non-neutral (i.e. diabatic) conditions accordingly, although this approximation might not be completely true. However, it is believed to be a fair approximation – alternatively the neutral case could be defined by the directly fitted values for L and Γ at the Høvsøre site, which is just another approximation to the Lillgrund conditions.

3.4.3 THE RESULTS

The results for the blade root equivalent moments and for the tower base for-aft equivalent moments are presented for the investigated ABL stability regimes in Figure 6 and in Figure 7, respectively.



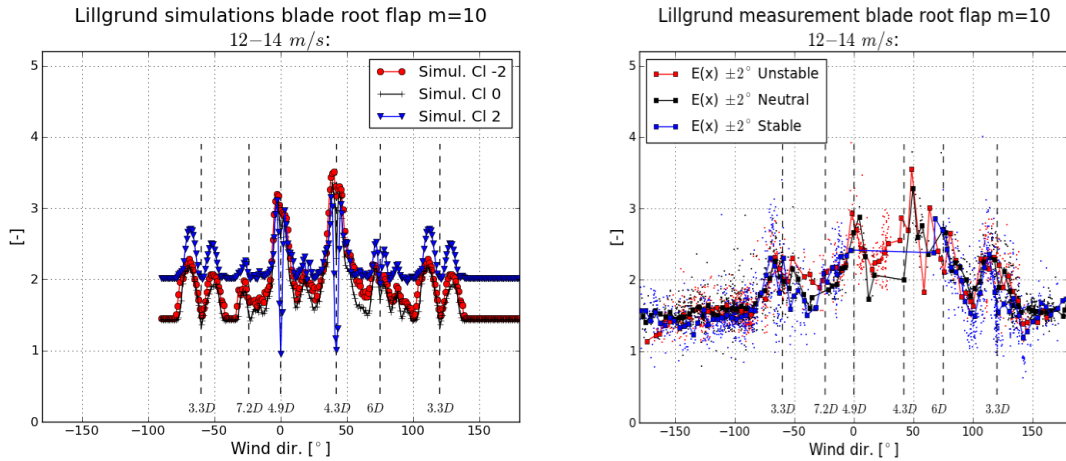
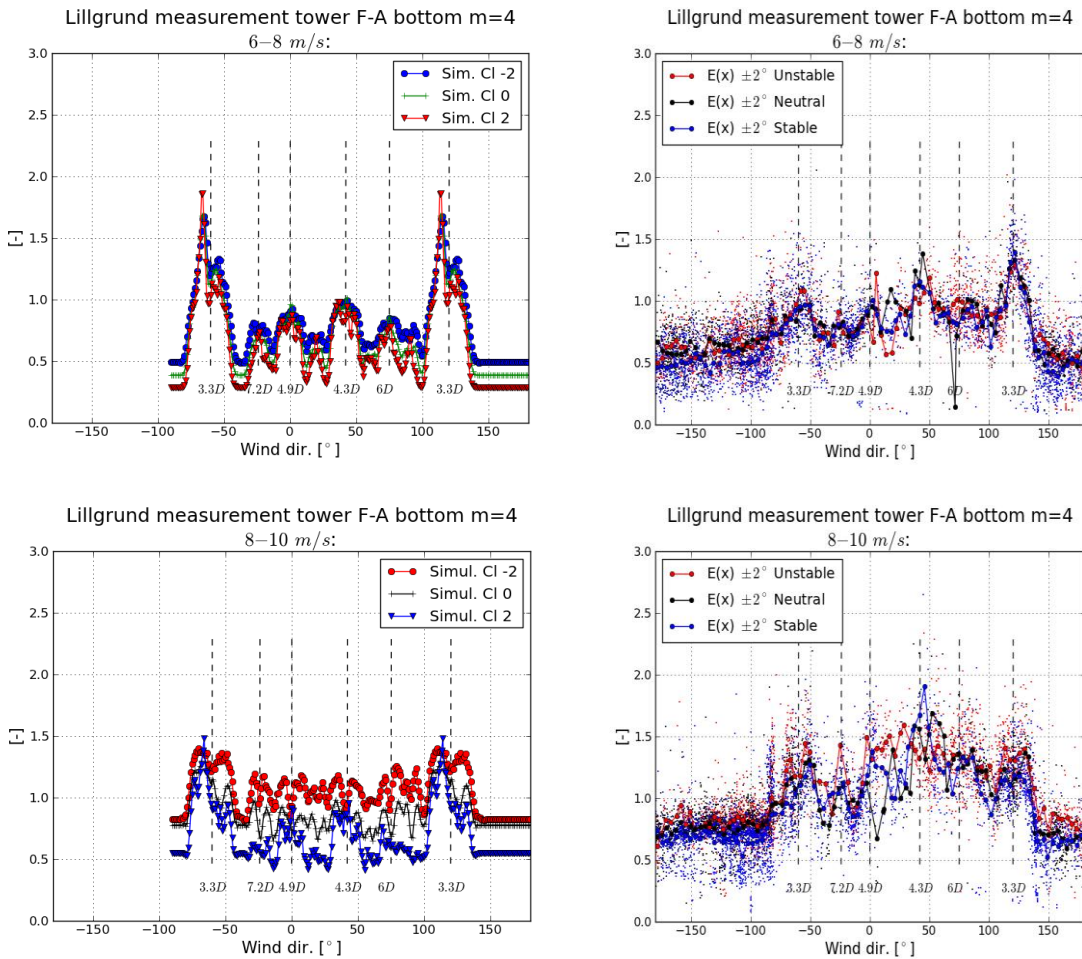


Figure 6: Comparison of measured and simulated blade flap fatigue loads for the C-8 WT. Solid markers connected by lines in the plots of the measured data represents direction bin specific mean values.



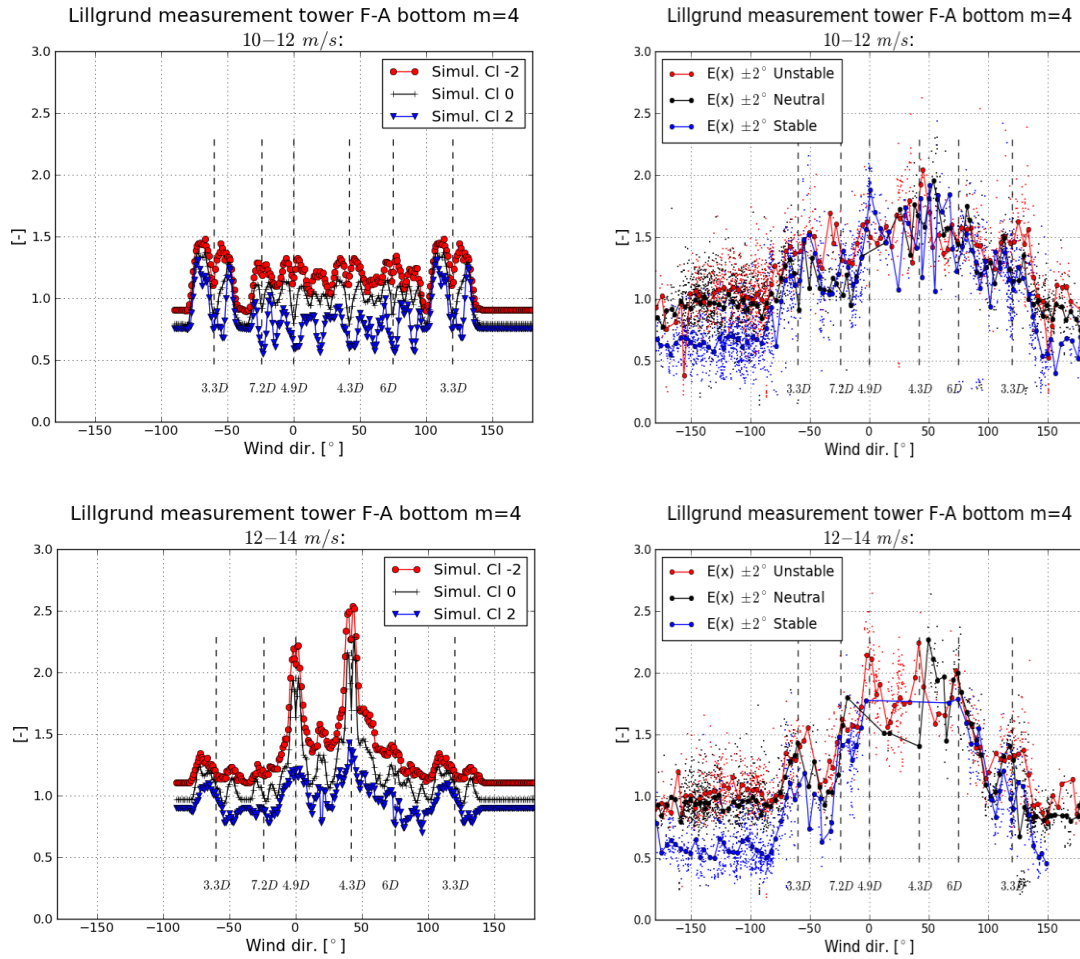


Figure 7: Comparison of measured and simulated tower bottom for-aft fatigue loads for the C-8 WT. Solid markers connected by lines in the plots of the measured data represents direction bin specific mean values.

For all wind speeds it can be seen that the *tower bottom fatigue bending moments* are largest in unstable and smallest in stable ABL conditions. This is explained by the difference in turbulence intensity associated with the investigated ABL stability conditions, where unstable conditions causes a turbulence level of 9.8%, neutral conditions corresponds to a turbulence level of 6.0%, and stable conditions corresponds to a turbulence level of 1.99%. The measured load levels are in general captured reasonable well by the simulations. However, the difference in fatigue load level caused by ABL stability effects are typically larger under multiple wake inflow situations in the simulations than seen from the measurements.

In the inflow sector 150deg. –180deg. the investigated WT is *not* affected by upstream wakes, and it is thus possible to evaluate the impact from ABL stability on solitary WT loading. When investigating the blade *flapwise fatigue loads* in this free sector, the results are significantly different from the tower fatigue loading. Contrary to tower loading, the blade loads are sensitive to both shear- and turbulence levels, as both cause varying wind speeds over the rotor area. For rotating WT components these are *counter acting effects*, because stable conditions result in large shear and low turbulence intensity and vice versa for unstable conditions. It is seen, that even with the mean wind speed profile modeled based the *extended M-O theory*, the impact from wind speed shear on the blade fatigue loading is still significantly over-estimated. One reason could be the crude classification of ABL stability applied in this investigation, since the M-O

correction formulated in eq. (14) is sensitive to the specific ABL stability condition - especially in the *below rated* mean wind speed regime (cf. Figures 4a and 4b). For most wind speeds, it is seen that the fatigue load level 'inside the WF' (i.e. corresponding to multiple wake inflow situations) is quite well predicted.

3.4.4 THE CONCLUSION

A medium-fidelity DWM/HAWC2 framework for modelling of wind turbine component fatigue loading, when the wind turbines are subjected to wake affected *non-stationary* flow fields under *non-neutral* atmospheric stability conditions, has been developed and demonstrated on full-scale load data from the Lillgrund WF. Compared to previous studies [24], a newly developed refinement of the classic M-O scaling theory was included in this study to account for un-realistic wind speed shears above the ABL surface layer under (strongly) stable stratification. This has reduced, but not removed, the over-prediction of blade fatigue loading of solitary WT's in (strongly) stable stratification.

A comparative analysis of measured and simulated blade and tower fatigue loads has revealed that ABL stability effects can explain a significant part of the large measurement scatter observed in full-scale data. The study has further gained insight in important load mechanism, and shown that vertical mean wind speed shear is the dominating fatigue load driver for the rotating WT components in stable ABL conditions, whereas turbulence (including its dictating wake meandering mechanism) is the dominating load driver for tower fatigue loading in general. Similar results were found in [25].

In a future perspective, the mean wind speed veer - also predicted by the extended M-O theory - will be included in the HAWC2/DWM model platform, as well as selected meso-scale effects. Finally, it is considered to consolidate the present Drogden based stability classification with WRF meso-scale simulations.

DWM IN FLOW FIELDS INFLUENCED BY WT YAWING

The 'classic' DWM model assumes Taylor advection of continuously 'emitted' wake deficit 'releases' in the longitudinal flow direction, which implies *flat and homogeneous terrain* with straight streamlines as well as neglect of the wake self-induced velocity field, which in turn facilitates de-coupling of the wake longitudinal kinematics from the wake transversal/vertical kinematics. Consequently, insignificant yaw errors (i.e. in principle zero yaw errors) are also implicitly assumed.

In the case of yawed WT operation, deflected wake patterns are seen. One of the first analyses such WF flow cases was Jiménez [20], who reported wake deflection caused yawed WT operation as based on CFD LES studies.

This Chapter is structured as follows: First deflected wake patterns and wake deficits are investigated using CFD modeling; then an indicative validation is performed by comparing with recent full-scale study; and finally the DWM model is generalized to account for yawed operation of WT's.

4.1 WAKE ADVECTION PATH AND WAKE DEFICIT

To get insights in flows behind WT's operating with a yaw error, detailed CFD simulations were performed including both Reynolds-averaged N-S (RANS) and Large Eddy Simulation (LES) type of simulations. In the following the numerical setup as well as the results of these investigations are described in some detail. The numerical studies are based on the in-house DTU EllipSys3D flow solver.

4.1.1 RANS BASED INVESTIGATIONS

EllipSys3D [26] is used to perform RANS simulations of the NREL-5MW reference WT [31] operating in various stationary yaw cases.

Model description

The wind turbine is represented as an Actuator Disk (AD) based on airfoil data [27, 28]. The RANS-AD setup is described in detail in previous work [29, 30], and only a summary will be presented here.

The NREL-5MW has a rotor diameter (D) and hub height of 126m and 90m, respectively. The inflow is assumed a neutral surface layer (logarithmic) profile with a roughness length of 0.03518m and a friction velocity of 0.4078m/s. This results in a wind speed and turbulence intensity at hub height of 8.0m/s and 10%, respectively. The flow domain is a Cartesian grid, which has dimensions of $800D \times 800D \times 10D$ in the streamwise, lateral and vertical directions. The inflow profile is in balance with the flow domain by using a rough wall boundary condition at the flat ground; an inflow boundary condition is used at the inlet and the top wall; an outlet condition is used at outflow boundary, at which fully developed conditions are assumed; and the lateral boundaries are periodic. Around the AD a refined domain is specified with dimensions $15D \times 6D \times 3D$, where the spacing is set to $D/20$. The total amount of cells is about 8.3 million. The AD is placed at $3D$ downstream of the start of the refined domain in both the streamwise and lateral directions. The turbulence is modeled by the $k-\epsilon-f_p$ model [29], which has been developed to simulate a wind turbine wake that compares well with large eddy simulation.

Results and discussion

A parametric study of yaw angles is simulated in the range of -30° to 30° with a 10° interval. Additional positive yaw angles of 5° , 15° and 25° are also simulated. A positive yaw angle is defined as a clockwise rotation as seen from above. Stream-wise velocity contours at downstream cross sectional planes normalized by the inflow profile are depicted in Figure 8. For positive and negative yaw angles, the wake deflects counter clockwise and clockwise, respectively. There is *no strong asymmetry* visible, other than a slight counter clockwise deflection, best seen for zero yaw, caused by the interaction of the wake rotation and the wind shear. Regarding the shape of the 'emitted' wake deficit - here represented by the 1D cross sectional plane deficits - it is noted that these, for the investigated flow case, are well represented by a rotational symmetric deficit for zero and moderate yaw errors (i.e. up to approximately 10°), whereas the wake deficit 'boundaries' seem slightly elongated/elliptic for larger yaw errors.

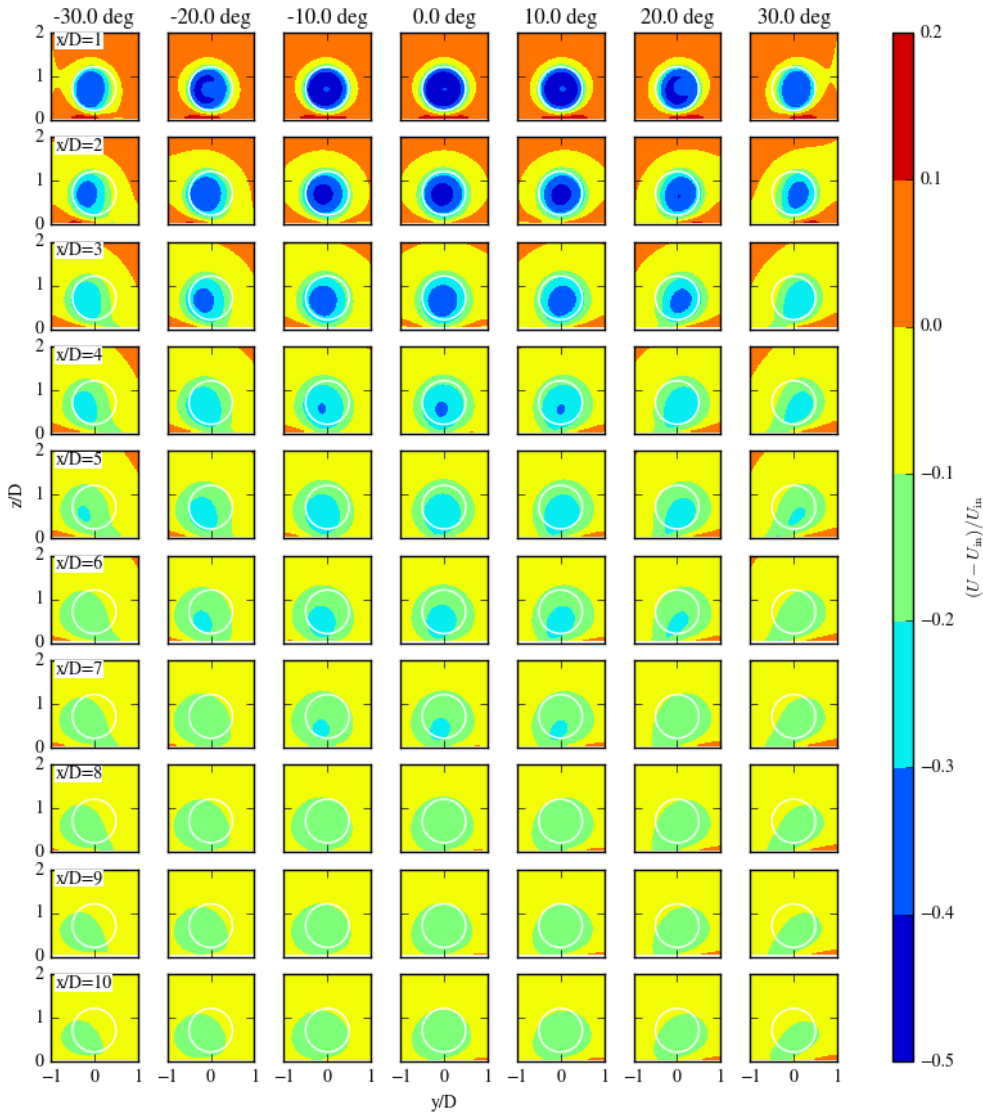


Figure 8: Downstream stream-wise velocity contours at vertical cross planes normalized by the inflow profile U_{in} of an AD operating in yaw. The AD is shown as a white circle.

Stream-wise velocity contours at hub height are plotted in Figure 9 for different yaw angles. A streamline (magenta line), which originates at the AD center, shows that for a yaw angle of 30° the wake center moves less than $0.5D$ in the lateral direction, at a downstream distance (x) of $10D$. The lateral wake deflection is also plotted in Figure 10 for yaw angles between 0° and 30° with a 5° interval for 5 downstream distances. Figure 10 shows that most of the wake deflection is obtained in the ‘first’ downstream distances (about 60-70% of the wake deflection at $x = 10D$ is achieved at $x = 4D$).

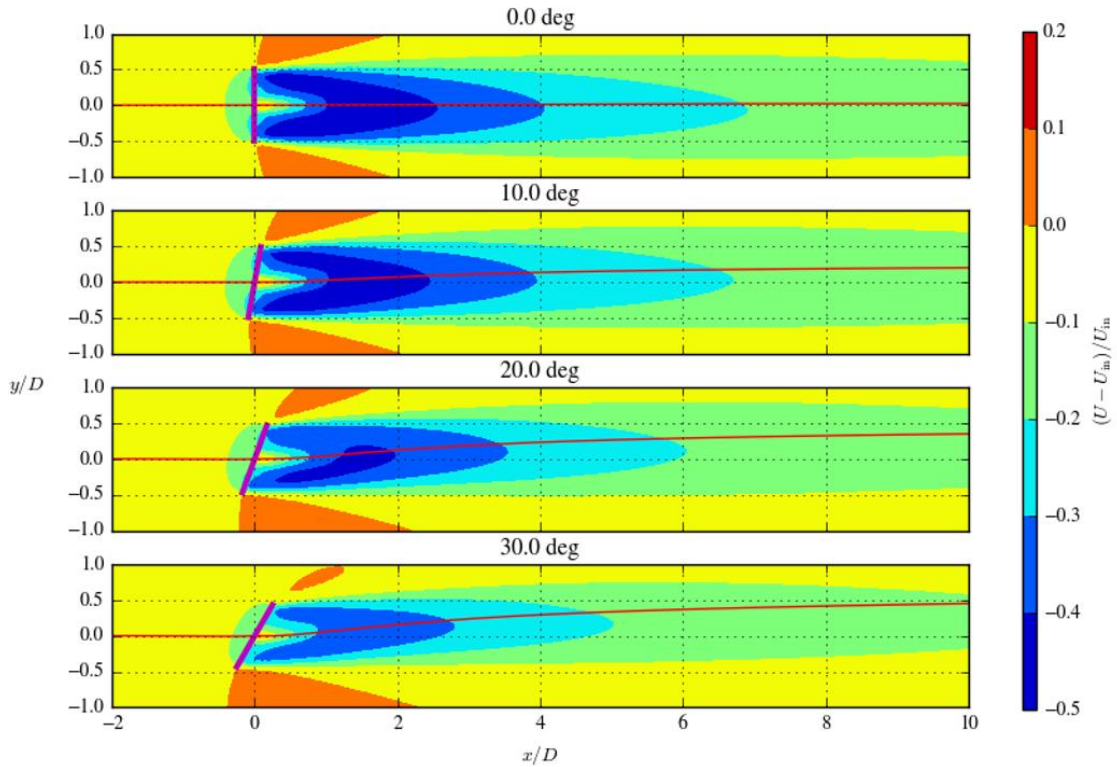


Figure 9: Stream-wise velocity contours normalized at hub height by the freestream of an AD operating in yaw. Magenta line is a streamline that originate from the AD center.

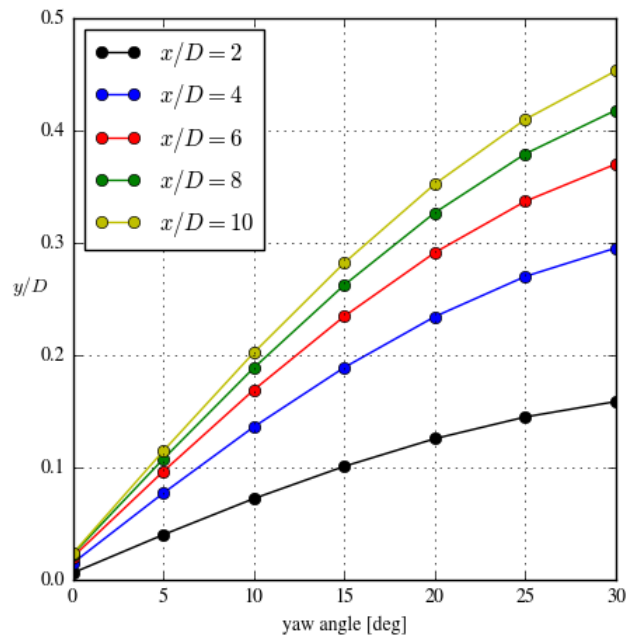


Figure 10: Lateral wake deflection as function of yaw angle and downstream distance. Wake deflection is based on a streamline that originates from the AD center.

The above RANS-based simulation of the curve-linear wake advection path's under yawed WT operation will be supplemented by a fast alternative based on a linear CFD approach (e.g. the DTU Fuga platform [32]). The work with generalizing Fuga to include WT's in yawed operation is in progress, and will be reported separately in D1.7.

4.1.2 LES BASED INVESTIGATIONS

As with the RANS simulations, the yawed WT and its wake is modelled using EllipSys3D, applying a block structured finite volume approach to solve the incompressible N-S equations. Contrary to the RANS computations, the WT is modelled using the actuator line methodology [33], and the WT is considerable smaller than the NREL-5MW reference WT - namely the Vestas V27 turbine.

Model description

The V27 WT has a hub height of 32m and a rotor diameter of 27m. The atmospheric boundary layer (i.e. shear as well as turbulence) is modeled by applying *body forces* throughout the domain. The investigated flow case is characterized by an undisturbed mean wind speed at hub height of 8.3m/s, inflow shear described by a power law with exponent 0.18 consistent with [7], and a turbulence intensity equal to 7.7%. The actuator lines representing the rotating WT blades are modeled using body forces defined using tabularized aerodynamic lift- and drag coefficients. Mann inflow turbulence was generated using parameters of $\alpha \varepsilon^{2/3} = 0.03379$, $L = 156.69\text{m}$ and $\tau = 3.0516$.

All simulations have been run on the same computational grid and with the exact same inflow conditions. With R denoting the rotor diameter, the grid is 60RX14RX40R in the stream-wise, lateral, and vertical directions, respectively. The grid contains a total of about 35 million cells. Inlet and outlet boundary conditions were used in the stream-wise direction, while cyclic boundary conditions were applied on the lateral boundaries. Far field boundary condition was applied at the top, while a no-slip condition was used on the bottom. The only change between simulations is the degree of yawing of the V27 WT. The simulations were run until 25 minutes of predictions were obtained.

Results and discussion

A parametric study is performed with yaw affected flow cases simulated for yaw angles of 0° , 5° , 15° , 25° , 30° and 35° . For these yaw cases, contours of the stream-wise time-averaged flow field component at hub height, normalized with the freestream inflow, are plotted in Figure 11. The wake location, used to define the yaw dictated wake deflection, is determined as locations with *maximum time-averaged wake deficit* at various downstream distances. This is different from the RANS study, where streamlines through the center of the wake generating rotor is used. In Figure 11 the red line represents lateral wake deflection. The lateral wake deflection is also plotted in Figure 12 as function of WT yaw angles for a variety of downstream distances ranging between 4 and 20 rotor radii (R). The scatter¹ in the results presented in Figure 12 indicates that, for the selected turbulence level, longer simulation times would most likely have been beneficial, and moreover that the selected wake deflection metric is not robust in especially the near wake regime, where bi-modal wake deficits prevail.

As expected the wake deflection increase with downstream distance as well as with the magnitude of the WT yaw error. With the selected metric, the wake deflection resulting from the LES investigation is in general moderately more pronounced than what was found using the

¹ This is e.g. illustrated by the fact, that the wake deflection, for the 15° yaw case, in average is larger at 4R downstream than at 8R downstream., which is not realistic.

RANS approach - although depending on the specific yaw case. However, in analogy with the RANS study we see that most of the wake deflection is obtained in the 'first' downstream distances. This is to be expected and for very large downstream distances, the gradient of the wake deflection should asymptotically approach zero.

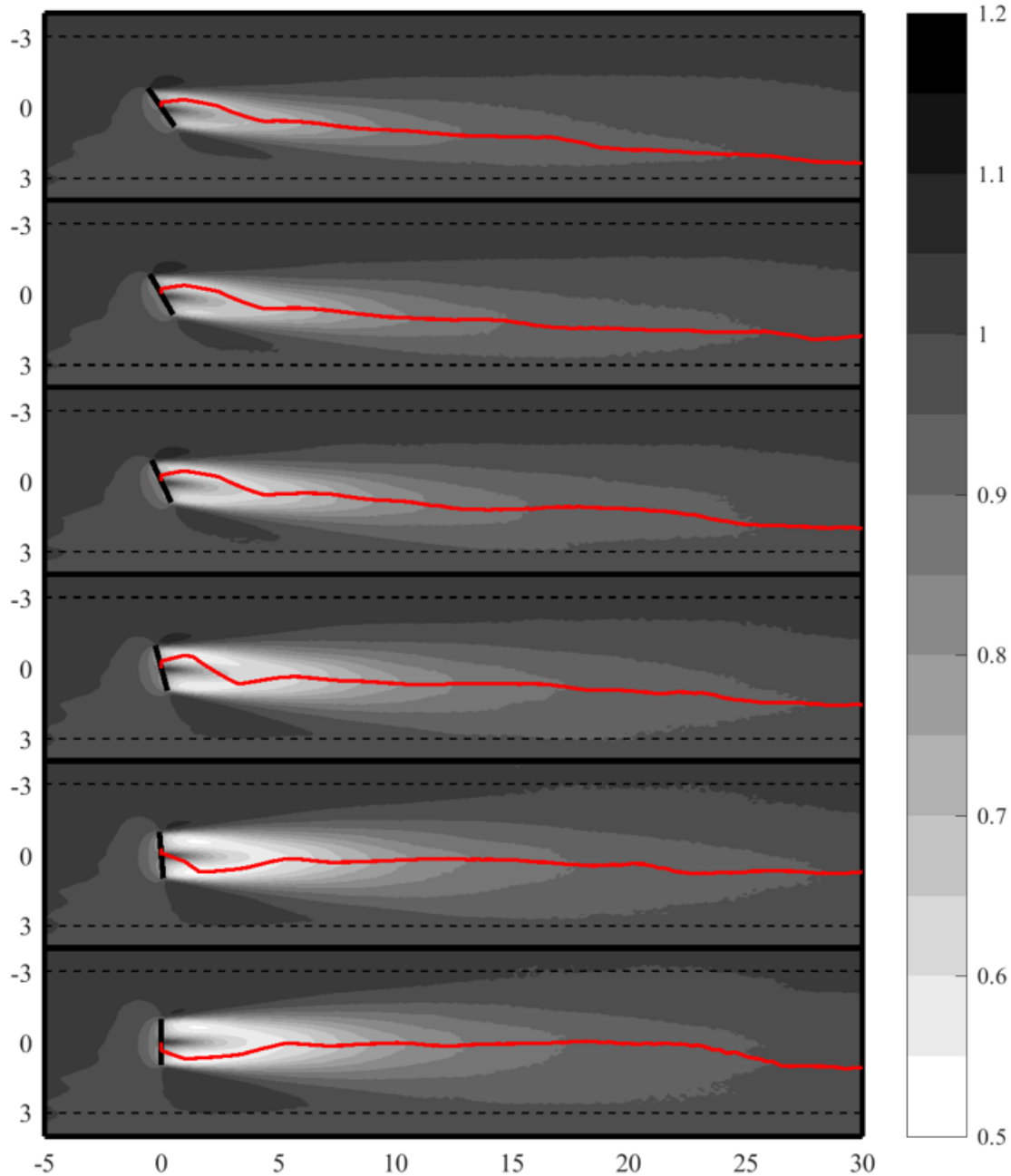


Figure 11: Stream-wise velocity contours normalized at hub height by the freestream inflow. Red line represents wake center location determined as minimum of the time averaged wake wind speed. For each of the six yaw vases the wake deflection [R] is shown as function of downstream distance [R].

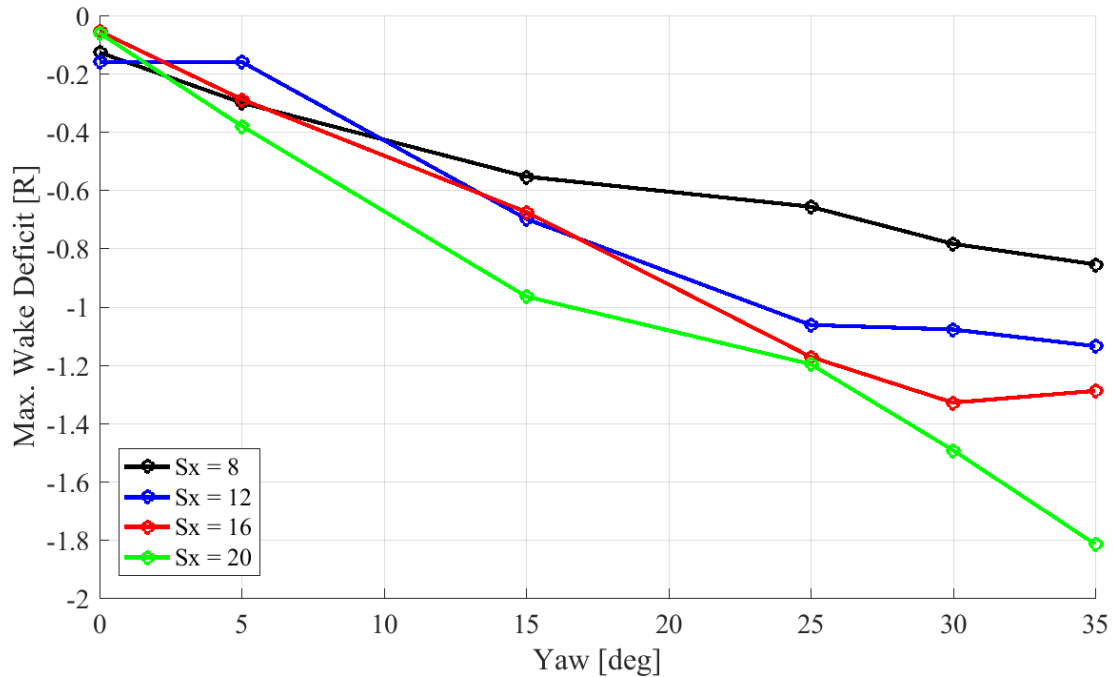


Figure 12: Lateral wake deflection as function of yaw angle and downstream distance, S_x , measured in R. Wake deflection is based on maximum time averaged wake deficit.

4.2 FULL-SCALE OBSERVATIONS OF FLOW FIELDS BEHIND A YAWED WT

A Vestas V52 turbine has been used for an intensive measurement campaign at the DTU-Risø campus during the fall 2018. This campaign is not a part of the TotalControl activities, but some of the findings are nevertheless relevant and can be used as an *indicative* validation of the above performed numerical studies.

The measurements comprise, among other things, a forward scanning spinner LiDAR as well as two ground based long-range WindScanner systems installed downwind of the turbine. The long-range WindScanner system [34], configured in dual-Doppler mode, scanned an area East of the turbine row (see Figure 13, left). During the analysis of these measurements, it was noticed that a special situation - a frontal passage - occurred on the 15th December at 11:50 (UTC+1), where the wind speed increased from 6m/s to 11m/s together with a fast accompanying change in wind direction of approximately 25° (see Figure 13, right).

The wake from the V52 WT is clearly identified in Figure 13. It is interesting to notice, that the direction of the wake is perfectly aligned with the ambient wind direction far downstream, but not in the near wake regime. The observed wake deflection in the near wake region seems to result from the instantaneous yaw error of the WT caused by the frontal passage. In this situation, the wake is misaligned with approximately 8° to 10° within a downstream distance of approximately 4D, resulting in a wake lateral deflection of approximately 0.5D. Although the flow case is not directly comparable with the flow cases analyzed in Section 4.1 (i.e. transient wind speed case, step-wise yawing WT, etc.) the experimental findings indicate, that the predicted lateral deflections patterns are qualitatively correct. It is also observed that the predicted maximum lateral wake deflections agree reasonable well with the experimental findings.

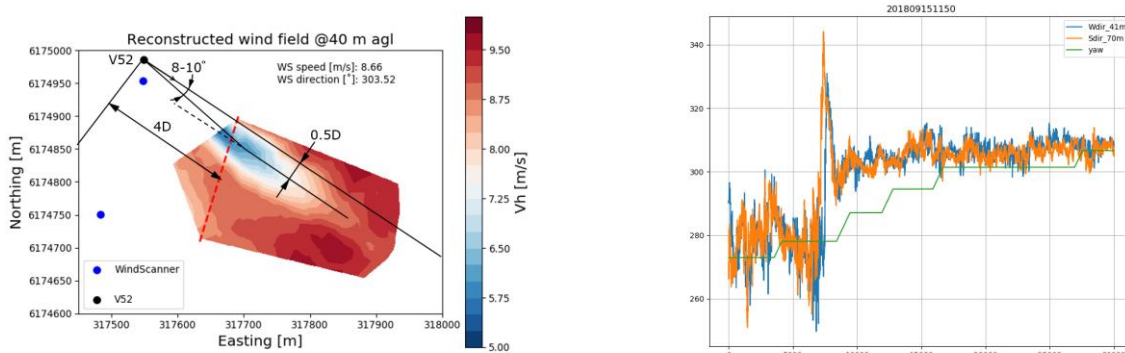


Figure 13: (Left) Measured wake of the V52 WT in a situation with yaw error; (Right) Wind direction at hub height 41m and at 70m measured on an upstream located meteorological mast.

4.3 DWM FOR YAWED OPERATION OF WT'S

To extend the applicability of the DWM model to yawed WT operational conditions, we will inherit the fundamental assumptions of the original model formulation and supplement these with new. Thus, we will assume moderate yaw errors up to of the order of 30° , because numerical investigations indicate that larger yaw errors do not seem to add significantly to wake deflection, but will add significantly to *increased loading and decreased production* of the yawed wake generating WT. This is further supported by Parkin [36], whose experimental results showed that the induced wake deflection flattens off for large yaw angles, thus giving a minimal gain in deflection by going to yaw angles beyond 30° .

We will describe the flow field in a Cartesian frame of reference, with the downstream coordinate directed along the ambient mean wind direction, a vertical coordinate in the direction of the gravity force, and a lateral coordinate defined in the direction of cross product of unit vectors in the two afore mentioned directions.

Wake advection

In case of yawed operation, the streamlines behind the wake generating WT will be curved in the near wake regime and asymptotically approaching straight lines in the far wake regime. Thus for the DWM approach generalized to yawed conditions, we will assume *mean* 'downstream' wake advection along the curved trace's defined by the flow streamlines - more precisely by the particular streamline through the rotor center of the wake generating WT. We will in the following denote this streamline the 'wake location streamline'. In analogy with the classic DWM approach [1], we will superimpose lateral- and vertical stochastic wake kinematics, dictated by large-scale turbulence structures in the ABL, linearly on the mean downstream wake advection path. Thus, an 'emitted' wake deficit is - like in the classic DWM model - assumed to exist in a 2D universe defined by the downstream advected cross section, in which the wake deficit 'release' was originally emitted. This cross section is assumed to be Taylor advected in the undisturbed mean wind direction with the undisturbed mean wind speed. In this cross section the kinematics of a wake 'release' will be described by a *mean deflection*², defined by the curvilinear 'wake location streamline' projected on this plane as the plane is advected downstream, linearly superimposed

² This is opposite to the classic DWM, where the mean deflection is zero.

by a time-integrated stochastic deflection defined by the large-scale turbulence characteristics of the cross section in question.

Being a medium-fidelity model, the individual components of the DWM model must also be medium-fidelity. Consequently, the ‘wake location streamline’ is determined based on RANS simulations - ultimately linear RANS simulations based on the generalized Fuga flow solver under development in D1.7. A through validation of RANS streamline prediction under yawed conditions can be done based on the dedicated full-scale LiDAR based measuring campaign on the Samsung 7MW turbine to be reported in D3.6.

Wake deficit

Classic DWM wakes are modeled as *circular symmetric* wakes based on a uniform, rotor averaged, inflow field. Thus, shear and rotational forces are not considered for the wake deficit modeling, which is justified by the approximate nature of the model, but certainly also by the extensive validation of the modeling framework conducted during recent years. As mentioned, this approach is not mandatory, but could also be modeled in more detail for example using a CFD actuator disc model and a sheared inflow field.

However, in analogy with the original simplified approach - and inspired by the CDF results presented in Chapter 3 - we will in the in adaptation of the DWM model to yawed WT operation exclude rotational forces and shear, and model the wake deficit as circular symmetric in a plane rotated the yaw angle, θ_y , around the vertical axis of the Cartesian frame of reference. The inflow, U_y , is again assumed uniform (i.e. rotor averaged) but modified compared to the zero yaw case inflow, U , as

$$U_y = U \cos \theta_y \quad (19)$$

thus implicitly assuming that only the inflow perpendicular to the rotor plane contribute to the rotor loading and thereby to the wake deficit. The modeled *circular symmetric* wake deficit field, $\Delta U(r, \theta, x)$, is expressed in a polar frame of reference - with r being the radius, x the downstream distance in the yawed Cartesian frame of reference and θ the azimuth angle - is finally transformed to a plane perpendicular to the undisturbed flow direction. Expressing the projected wake deficit, $\Delta U'(r', \theta', x')$, in another polar frame of reference, (r', θ', x') , we find

$$\Delta U' \left(\frac{r'}{2} [1 + \cos \theta_t] + \frac{r' \cos 2\theta'}{2} [1 - \cos \theta_t], \theta', x' \right) = \Delta U(r', \theta', x') \quad (20)$$

with transformation angle, θ_t , given by

$$\theta_t = \tan^{-1} \left(\frac{y_w}{x} \right) \quad (21)$$

where y_w is the lateral wake deflection at distance x caused by the WT yaw error. The transformation angle is equal to the yaw error for $x = 0$ and decreases asymptotically to zero for very large distances x . Note that in the DWM model, the deficit field, $\Delta U(r, \theta, x)$, expands and attenuates with the downstream distance reflecting the small scale diffusion of the deficit in the meandering frame of reference. The mapping described in eq. (20) results in elliptic wake deficits for yaw operation and the traditional circular symmetric wake deficit for zero yaw.

Wake self-generated turbulence

With reference to Figure 1, the last DWM component to be considered is the wake self-generated small-scale turbulence. As the characteristic scale of this small-scale turbulence field is comparable with the characteristic size of the wake deficit, we will, in analogy with the classic

DWM formulation, formulate this turbulence field in the meandering frame of reference. We will further adapt the original scaling approach, where simple scaling of a homogeneous and isotropic turbulence field approximates the *circular symmetric* induced turbulence, although thereby somewhat violating the second order statistics of the field. Modeling the turbulence field in the same plane as the rotational symmetric deficit, the only difference compared to classic DWM is the scaling [10]. The scaling depends on the wake deficit magnitude, which in turn depends on the modified inflow conditions expressed in eq. (19).

The wake self-generated turbulence field, formulated in the a plane perpendicular to the undisturbed flow direction, will finally be approximated by transforming the modeled circular symmetric small-scale turbulence field, $\mathbf{u}(r, \theta, x)$, to this frame of reference. Adapting the notation from the wake deficit modeling with $\mathbf{u}'(r', \theta', x')$ denoting the small-scale turbulence field in a polar system in a plane perpendicular to the undisturbed mean wind direction, we find

$$\mathbf{u}'\left(\frac{r'}{2}[1 + \cos \theta_t] + \frac{r' \cos 2\theta'}{2}[1 - \cos \theta_t], \theta', x'\right) = \mathbf{u}(r', \theta', x') . \quad (22)$$

CONCLUSIONS

To account for loading in the context of WF control requires non-stationary modelling of the WF flow field. High-fidelity LES CFD is capable to model such non-stationary flow fields but is, due to the massive CPU requirements, not suited for design of *optimized* WF control schemes, where a large number of flow simulations are needed.

This in turn calls for suitable medium-fidelity and/or engineering low order modelling approaches. The DWM model is a ‘mature’ representative of the medium-fidelity model class, which has recently been included as a recommended practice in the IEC code [7].

The first version of this model complex was tailored to neutral ABL stability conditions and assumed zero yaw error of the WF WT’s. However, WT loading depends on ABL stability, and therefore it is important to extend the capability of the DWM model to also account for non-neutral ABL conditions. The generalization of the DWM model to such conditions is described Chapter 3 of this report along with a full-scale validation case based on measurements from the Lillgrund WF.

To optimize WF control, individual WT de-rating and individual WT wake-steering (i.e. WT yaw control) are the traditional approaches. The standard DWM model is capable of handling the de-rating strategy, while the yaw control requires a generalization of the standard model. This is dealt with in Chapter 4 of this report, where a generalization of the model is formulated. Prior to the model formulation, various numerical high-fidelity studies are conducted followed by an ‘indicative’ validation of these.

REFERENCES

1. Larsen GC, Madsen HAa, Larsen TJ and Thomsen K (2008). Wake meandering - a pragmatic approach. *Wind Energy*; **11**(4): 377–395.
2. Bingöl F, Mann J and Larsen GC (2010). Light detection and ranging measurements of wake dynamics. Part I: one-dimensional scanning. *Wind Energy*, **13**(1), pp. 51–61.
3. Trujillo J, Bingöl F, Larsen GC, Mann J and Kühn, M (2011). Light detection and ranging measurements of wake dynamics. Part II: two-dimensional scanning. *Wind Energy*, **14** pp. 61–75.

4. Macheaux E, Larsen GC, Troldborg N, Gaunaa M and Rettenmeier A (2015). Empirical modeling of single-wake advection and expansion using full-scale pulsed lidar-based measurements. *Wind Energy*, **18**, pp. 2085–2103.
5. Larsen TJ, Madsen HAa, Larsen GC and Hansen KS (2012). Verification of the Dynamic Wake Meander Model for Loads and Power Production in the Egmond aan Zee Wind Farm. *Wind Energy*, **16**, pp. 605–624.
6. Larsen TJ, Larsen GC, Madsen HAa, Thomsen K and Pedersen SM (2015). Wake effects above rated wind speed - An overlooked contributor to high loads in wind farms. *Scientific Proceedings, EWEA Annual Conference and Exhibition 2015*, pp. 95-99.
7. IEC 61400-1. Wind turbines—part 1: Design requirements
8. J.C. Kaimal and J.J. Finnigan (1994). *Atmospheric Boundary layer Flows – Their structure and Measurement*. Oxford University Press.
9. J. Mann (1994). The Spatial Structure of Neutral Atmospheric Surface-Layer Turbulence. *J. of Fluid Mech.*, **273**, pp. 141-168.
10. Madsen HAa, Larsen GC, Larsen TJ and Troldborg N (2010). Calibration and Validation of the Dynamic Wake Meandering Model for Implementation in an Aeroelastic Code. *J. Sol. Energy Eng.*, **132**(4).
11. Larsen GC et al. (2007). Dynamic wake meandering modeling. Risø-R-1607(EN), Risø National Laboratory, Roskilde.
12. Macheaux E, Larsen GC, Tilman K, Troldborg N, Kelly MC, Chougul A, Hansen KS and Rodrigo JS (2016). An experimental and numerical study of the atmospheric stability impact on wind turbine wakes. *Wind Energy*, **19**, pp. 1785–1805.
13. Chougule A, Mann J, Kelly MC and Larsen GC (2016). Modeling atmospheric turbulence via rapid-distortion theory: spectral tensor of velocity and buoyancy. *Journal of the Atmospheric Sciences*, Vol. **74**, Issue 4, pp. 949–974.
14. Chougule A, Mann J, Kelly MC and Larsen GC (2016). Validation of buoyancy driven spectral tensor model using HATS data. *Journal of Physics: Conference Series (Online)*, Vol. **753**, No. 3, 032038.
15. Chougule A, Mann J, Kelly MC and Larsen GC (2017). Simplification and Validation of a Spectral-Tensor Model for Turbulence Including Atmospheric Stability. *Boundary-Layer Meteorology*, Vol. **167**, Issue 3, pp. 371–397.
16. von Kármán, T. (1948). Progress in the statistical theory of turbulence. *Proc. Nat. Acad. Sci.*, **34**, pp.530–539.
17. Mann, J. (1998). Wind field simulation, *Prob. Eng. Mech.* **13**(4), pp. 269–282.
18. Gryning S-E et al. (2007). On the extension of the wind profile over homogeneous terrain beyond the surface layer. *Boundary-Layer Meteorology* **124**, pp. 251–268.
19. Miner MA (1945). Cumulative damage in fatigue. *Journal of Applied Mechanics*, **12**, pp. 159–164.
20. Jiménez A, Crespo A and Migoya E (2010), Application of a LES technique to characterize the wake deflection of a wind turbine in yaw. *Wind Energy 2010*, vol. **13**, pp. 559-572.
21. Larsen GC, Ott S, Larsen TJ, Hansen KS and Chougule A (2018). Improved modelling of fatigue loads in wind farms under non-neutral ABL stability conditions. *IOP Conf. Series: Journal of Physics. The Science of Making Torque from Wind (TORQUE 2018)*.
22. Larsen GC, Ott S, Troldborg N, Chougule A, Mann J, Macheaux E, Verelst DR, Larsen TJ, Mirzaei M, Bertagnolio F, Kelly M, Hansen, KS and Marion L (2016). Impact of atmospheric stability conditions on wind farm loading and production. *DTU Wind Energy E-0136(EN)*, 140 p.

23. IEC 61400-3. Wind turbines – part 1: Design requirements for offshore wind turbines, 2009.
24. Larsen GC, Larsen TJ and Chougule A. (2017). Medium fidelity modeling of loads in wind farms under non-neutral ABL stability conditions – a full-scale validation study. [Journal of Physics: Conference Series \(Online\)](#), 854, 012026.
25. Sathe A, Mann J, Barlas T, Bierbooms WAAM and van Bussel GJW (2013). Influence of atmospheric stability on wind turbine loads. *Wind Energy*, Vol. 16, Issue 7, pp. 1013–1032.
26. Michelsen JA. (1992). Basis3d - a platform for development of multiblock PDE solvers. Technical University of Denmark, Lyngby, Denmark, Tech. Rep. AFM 92-05.
27. Mikkelsen R (2003). Actuator Disc Methods Applied to Wind Turbines. Ph.D. dissertation, Technical University of Denmark, Mech. Dept, Lyngby, Denmark.
28. Réthoré P-E, van der Laan MP, Troldborg N, Zahle F and Sørensen NN (2014). Verification and validation of an actuator disc model. *Wind Energy*, vol. 17, pp. 919–937.
29. van der Laan MP, Sørensen NN, Réthoré P-E, Mann J, Kelly MC, Troldborg N, Schepers JG and Machefaux E (2015). An improved k- ϵ model applied to a wind turbine wake in atmospheric turbulence. *Wind Energy*, vol. 18, no. 5, pp. 889–907.
30. van der Laan MP, Sørensen NN, Réthoré P-E, Mann J, Kelly MC and Troldborg N (2015). The k- ϵ - fp model applied to double wind turbine wakes using different actuator disk force methods. *Wind Energy*, vol. 18, no. 12, pp. 2223–2240.
31. Jonkman J, Butterfield S, Musial W and Scott G (2009). Definition of a 5-MW Reference Wind Turbine for Offshore System Development. National Renewable Energy Laboratory, Tech. Rep.
32. Ott S, Berg J and Nielsen M (2011). Linearized CFD models for wakes. Risø-R-1772(EN). Risø National Lab. for Sustainable Energy, 39p.
33. Sørensen JN and Shen WZ (2002). Numerical modelling of Wind Turbine Wakes. *J. Fluids Eng.*, 124, 393–399.
34. Vasiljevic N, Lea G, Courtney M, Cariou J-P, Mann J and Mikkelsen TK (2016). Long-Range WindScanner System. Remote Sensing, 8(11). DOI: 10.3390/rs8110896.
35. Paulson CA (1970). The mathematical representation of wind speed and temperature profiles in the unstable surface layer. *J. Appl. Meteor.*, 9, 857-861.
36. Parkin P, Holm R and Medici D (2001). The application of PIV to the wake of a wind turbine in yaw. Proc. 4th International Symposium on particle image Velocimetry, Göttingen.